GEOPHYSICAL RESEARCH LETTERS, VOL. 31, L24608, doi:10.1029/2004GL021569, 2004

Global and local isostatic coherence from the wavelet transform

J. F. Kirby and C. J. Swain

Western Australian Centre for Geodesy, Curtin University of Technology, Perth, Western Australia, Australia

Received 20 September 2004; revised 3 November 2004; accepted 29 November 2004; published 23 December 2004.

[1] A method to compute the variations in lithospheric elastic thickness (T_e) has been developed, using the wavelet transform. The technique, which uses a superposition of two-dimensional Morlet wavelets in a geometry named a 'fan' wavelet, is designed to yield isotropic yet complex wavelet coefficients for the co- and cross-spectra of gravity and topography data. These are then used to compute a spatially-varying, isostatic coherence, from which both global and local estimates may be obtained. We applied the method to synthetic gravity and topography generated for a thin elastic plate of uniform thickness 20 km, yielding an apparent, spatially variable T_e of 24.5 ± 3.5 km. The estimated global coherence for this model appears to fit the theoretical prediction as well as Fourier transform-based estimates, and is smoother than these. We also computed the wavelet coherence, and hence spatially-varying T_e, for a plate of non-uniform thickness, yielding a difference with the model of −2.0 ± 1.7 km. *INDEX TERMS:* 1236 Geodesy and Gravity: Rheology of the lithosphere and mantle (8160); 8110 Tectonophysics: Continental tectonics—general (0905); 8159 Tectonophysics: Rheology—crust and lithosphere. **Citation:** Kirby, J. F., and C. J. Swain (2004), Global and local isostatic coherence from the wavelet transform, *Geophys. Res. Lett.*, *31*, L24608, doi:10.1029/2004GL021569.

1. Introduction

[2] Spectral isostatic analysis involves estimation of two 'spectral parameters': the admittance and coherence between the observed gravity field and topography over a region. These two quantities are usually determined in the wavenumber domain through the Fourier transform, and are essentially measures of the correlation between gravity and topography. Once the admittance and coherence have been estimated, it is possible to determine the effective elastic thickness of the lithosphere in that region, as well as the ratio of subsurface to surface loading (f), by comparing the observed spectral parameters with theoretical curves predicted from various plate models. However, the current thrust of isostatic research is concerned with estimation of the spatial variation of T_e between provinces [e.g., *Lowry and Smith*, 1994; *Poudjom Djomani et al.*, 1999], and the Fourier transform is particularly unsuited to this task. For many years, T_e variations were determined by Fourier transforming within a moving window, but more recently using the methods of maximum entropy [*Lowry and Smith*, 1994] and multitapers [*McKenzie and Fairhead*, 1997], to compute the two-dimensional (2D) admittance and coherence. However, these methods often yield unreliable T_e estimates owing to the fact that the window size is not large enough to resolve the long wavelengths of interest to researchers, and also because multitapers bias results [*Swain and Kirby*, 2003]. Such is the dilemma facing us: mapping T_e with small windows does not yield information in the long wavelengths; while mapping using large windows will not yield T_e variations.

[3] Here, we suggest the use of the continuous wavelet transform (CWT) for estimating spatial admittances and coherences, and hence for mapping the spatial variations of T_e. Essentially, the CWT enables a power spectrum to be computed at every node of a data grid, as opposed to the Fourier transform, which can only yield one spectrum for the whole grid. It is therefore possible to estimate the isostatic admittance and coherence at every grid node, and thus estimate the spatial variation of T_e by comparison with theoretical models, as mentioned earlier.

[4] The concept of wavelet admittances and coherences has previously been employed by *Stark et al.* [2003] who used the Derivative of Gaussian (DoG) wavelet to determine the variations of effective elastic thickness (T_e) in southern Africa. However, we believe the technique employed here is superior to this earlier study as it succeeds not only in improving upon Fourier-based estimates, but also in accurately reproducing the theoretical admittances and coherences predicted by uniform plate models. The improvement lies in a better choice of wavelet, based upon a controlled superposition of Morlet wavelets, dubbed the 'fan wavelet'. The advantage in using the Morlet wavelet as a base is that it is a Gaussian-modulated complex exponential (in the space-domain), possessing similar properties to the Fourier transform itself. It has been found that the wavelet power spectrum ('scalogram') from the Morlet wavelet almost exactly reproduces the radially-averaged Fourier periodogram, whereas the scalograms from other wavelets do not hold this property [*Kirby*, 2004].

2. The Wavelet Coherence

[5] The ability of the CWT to estimate local power spectra is achieved through the use of localised basis functions (wavelets), rather than the infinitely-repeating complex exponentials of Fourier analysis. The CWT of a 2D spatially-distributed signal, $g(\mathbf{x})$, is computed from the convolution of the signal with the complex conjugate of a wavelet; or, via the Fourier transform as:

$$\tilde{g}(s, \mathbf{x}, \theta) = \mathbf{F}^{-1}\left\{\hat{g}(\mathbf{k})\hat{\psi}^{*}_{s,\theta}(\mathbf{k})\right\} \quad (1)$$

Here, the $\tilde{g}(s, \mathbf{x}, \theta)$ are the resulting 'wavelet coefficients'; s is the scale, determining the width (dilation) of the wavelet and hence resolution; θ is the rotation parameter, determining the resolving azimuth of the wavelet. Also, $\mathbf{k} = (u, v)$ is

0094-8276/04/2004GL021569$05.00

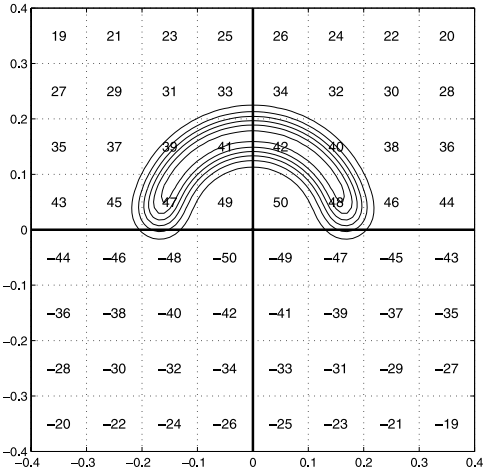

Figure 1. The imaginary part of the Fourier transform of some real-valued data, multiplied by a fan wavelet.

the 2D wavenumber; $\mathbf{F}^{-1}$ is the inverse 2D Fourier transform; and $\hat{g}(\mathbf{k})$ is the 2D Fourier transform of the signal. The $\hat{\psi}^*_{s,\theta}(\mathbf{k})$ is the complex conjugate of the 2D Fourier transform of the 'daughter' wavelets. These are dilated, translated and rotated versions of a 'mother' wavelet, $\hat{\psi}(\mathbf{k})$, with:

$$\hat{\psi}_{s,\theta}(\mathbf{k}) = s\,\hat{\psi}\left(s\Omega^{-1}(\theta)\mathbf{k}\right) \tag{2}$$

The rotation matrix, $\Omega(\theta)$, belongs to the SO(n) group [*Farge*, 1992]. For a full discussion of the 2D CWT, the reader is referred to *Farge* [1992].

[6] For the purposes of isostatic investigations, the analyzing wavelet must be able to generate complex (rather than real-only) wavelet coefficients, otherwise the coherence always takes a value of unity. Furthermore, the wavelet should be isotropic so as to utilize all available data: an anisotropic wavelet will only resolve features aligned in a particular direction, depending upon the orientation of the wavelet. However, while real wavelets, such as the DoG, are isotropic, they will not generally generate complex wavelet coefficients. And complex wavelets, such as the Morlet, are not isotropic, yielding coefficients resolved only along a certain azimuth. It is, however, possible to generalise the Morlet wavelet by superposition so that it does yield isotropic and complex wavelet coefficients. This is achieved by considering the redundancy of information in the wavenumber domain.

[7] Consider the mechanics of taking the wavelet transform of real-valued data using a superposition of Morlet wavelets. Firstly, the Fourier transform of an asymmetric distribution of real-valued data is a 'Hermitian' function, with an even real part, and an odd imaginary part [*Bracewell*, 1986]. Figure 1 shows a schematic diagram of the values taken by the imaginary part of the Fourier transform of some data. If the upper-right quadrant in the wavenumber domain contains some distribution of numbers, **A**, and the upper-left quadrant contains **B**, then the lower quadrants are just negative reflections of these, $-\mathbf{A}$ and $-\mathbf{B}$, and hence contain redundant information.

[8] Superimposed upon these quadrants in Figure 1 is a half-annulus, representing multiplication by a superposition of Morlet wavelets, dubbed a 'fan' wavelet. As shown, the fan wavelet spans the whole of the upper two quadrants, which is all that is necessary to achieve isotropy. Furthermore, as it has an asymmetric Fourier transform, it is a Hermitian function in the space-domain, thus generating complex wavelet coefficients.

[9] The basis for the fan wavelet is the 2D Morlet wavelet, which has Fourier transform:

$$\hat{\psi}(\mathbf{k}) = e^{-\left[(u-|\mathbf{k}_0|\cos\theta)^2+(v-|\mathbf{k}_0|\sin\theta)^2\right]/2} \tag{3}$$

where $|\mathbf{k}_0| = \pi\sqrt{2/\ln 2} \approx 5.336$ is required to ensure the admissibility condition is (almost) met [e.g., *Farge*, 1992], and θ is the angle made with the positive u-axis. The scale of each daughter wavelet (equation (2)) can be related to an 'equivalent Fourier wavenumber', k_F, by taking the wavenumber at which the wavelet has its maximum value (for that scale) to be representative of the harmonics resolved by the wavelet. For the Morlet wavelet, this relationship is

$$k_F = \frac{|\mathbf{k}_0|}{s} \tag{4}$$

This procedure then enables direct comparison with Fourier spectra.

[10] The 2D wavelet coherence is computed by summing the wavelet cross- and co-spectra at different azimuths:

$$\gamma^2_W(s,\mathbf{x}) = \frac{\left|\left\langle \tilde{g}_{s\mathbf{x}\theta}\,\tilde{h}^*_{s\mathbf{x}\theta}\right\rangle_\theta\right|^2}{\left\langle \tilde{g}_{s\mathbf{x}\theta}\,\tilde{g}^*_{s\mathbf{x}\theta}\right\rangle_\theta \left\langle \tilde{h}_{s\mathbf{x}\theta}\,\tilde{h}^*_{s\mathbf{x}\theta}\right\rangle_\theta} \tag{5}$$

where, the $\tilde{g}_{s\mathbf{x}\theta}$ are the Bouguer anomaly wavelet coefficients from one Morlet wavelet transform at a certain azimuth θ, and the $\tilde{h}_{s\mathbf{x}\theta}$ are those of the topography. Each Morlet wavelet is normalised so that its energy at each scale is constant.

[11] The superposition of Morlet wavelets into a fan-geometry is achieved by azimuthal averaging, denoted by $\langle\cdot\rangle_\theta$. The azimuthal separation between adjacent Morlet wavelets in the wavenumber domain is given by $\delta\theta = 2\sqrt{-2\ln p}/|\mathbf{k}_0|$, where p represents the amplitude at which adjacent bell-curves intersect ($0 < p < 1$). The optimal value for p was determined to be 0.75, giving a fan wavelet geometry as shown in Figure 1.

[12] Hence, the cross- and co-spectra are computed separately at all allowed values of θ from 0° to 180°, and then averaged according to equation (5), yielding a wavelet coherence that is two-dimensional and isotropic.

[13] It should be noted that, with this arrangement, it is possible to constrain the range of θ so that anisotropic estimates of the admittance and coherence can be obtained, in any azimuth.

[14] A further point of note is the difference between 2D coherences computed through, for example, the method of multitapers, and the presented wavelet coherence. The multitaper method yields $\gamma^2(\mathbf{k})$, or the coherence of the whole region as a function of 2D wavenumber. The wavelet coherence, $\gamma^2_W(s, \mathbf{x})$, is a function of space and wavelength (by virtue of scale), providing one-dimensional (1D) coherence profiles at each grid node.

[15] However, the wavelet method can also yield a global 1D profile, through an averaging over the space variable, $\mathbf{x}$ (and represented by $\langle\cdot\rangle_{\mathbf{x}}$), for each scale. This is useful for comparison with theoretical models for uniform plates. The global wavelet coherence is thus:

$$\overline{\gamma_W^2}(s) = \frac{\left\langle \left\langle \tilde{g}_{s\mathbf{x}\theta}\, \tilde{h}^*_{s\mathbf{x}\theta} \right\rangle_\theta \right\rangle_{\mathbf{x}} \left\langle \left\langle \tilde{g}_{s\mathbf{x}\theta}\, \tilde{h}^*_{s\mathbf{x}\theta} \right\rangle_\theta^* \right\rangle_{\mathbf{x}}}{\left\langle \left\langle \tilde{g}_{s\mathbf{x}\theta}\, \tilde{g}^*_{s\mathbf{x}\theta} \right\rangle_\theta \right\rangle_{\mathbf{x}} \left\langle \left\langle \tilde{h}_{s\mathbf{x}\theta}\, \tilde{h}^*_{s\mathbf{x}\theta} \right\rangle_\theta \right\rangle_{\mathbf{x}}} \tag{6}$$

which is now a function of scale only. Direct comparison with theoretical coherence curves is then made by converting scale to equivalent Fourier wavenumber through equation (4).

[16] It should be noted that it is also possible to compute both a wavelet admittance, $Q_W(s, \mathbf{x})$, and global wavelet admittance using the fan wavelet.

3. Application to Synthetic Data

[17] The method was tested on synthetic data sets generated from fractal surface and subsurface loads imposed on a thin elastic plate [*Macario et al.*, 1995]. We used the model of *Forsyth* [1985] with loads at the surface and Moho whose weights are in the ratio 1:f. The loads were generated by the Spectral Synthesis method [*Peitgen and Saupe*, 1988], using the fast Fourier transform (FFT). For uniform plates we also calculated the flexure via the FFT [*Macario et al.*, 1995]. For non-uniform plates we solved the differential equation by finite differences (FD) using sparse matrix techniques [*Stark et al.*, 2003], with periodic boundary conditions. *Stewart* [1998] compared such solutions for a uniform plate with the corresponding FFT results and found differences of <1%. Initially we followed *Stewart* [1998] in solving the FD equations for small grids ($N_x \times N_y = 128 \times 128$) using a direct LU method. However we have found that the conjugate gradient method [*Press et al.*, 1992] gives accurate solutions for larger grids in much less time. Since the number of unknowns varies as $(N_x N_y)^2$, this is important.

[18] Our initial result shows the global wavelet coherence estimates, as a function of equivalent Fourier wavenumber, of a pair of synthetic grids generated for a uniform plate of T_e = 20 km, f = 1 (Figure 2). Periodogram estimates of coherence are also shown in Figure 2 along with values calculated from the analytical formula [e.g., *Pérez-Gussinyé et al.*, 2004]. It can be seen that wavelet and periodogram estimates agree well, but that the wavelet estimates are smoother. We assert that this statement is generally true, from the large set of such results that we have generated for a range of different T_e and f values and initial random number "seeds". Figure 2 shows a case where both methods agree very well with the theoretical curve, but due to the random variation inherent in the fractal loads used to generate the synthetic data the fit is not always so good. This means that T_e estimates made from both wavelet and Fourier coherences may deviate from the values used to generate the data. We find that the standard deviation (SD) of such variations in the wavelet approach is typically ~10–20%, similar to that found by *Macario et al.* [1995] for periodogram estimates.

[19] The above characteristic of the fan wavelet gives it an important advantage over the one used by *Stark et al.* [2003]. They had to use numerical integration to generate model curves, because their wavelet coherence was not a particularly close approximation to the Fourier coherence.

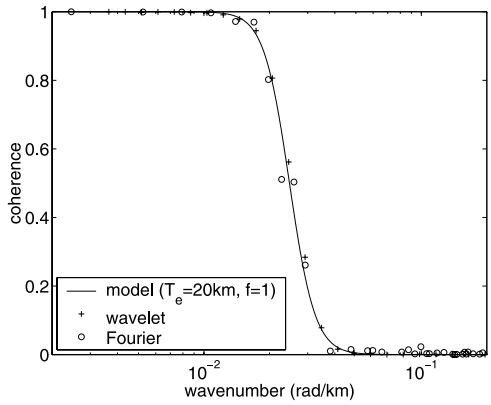

Figure 2. Theoretical coherence for a uniform thin elastic plate model with T_e = 20 km, f = 1 (solid line), together with numerical estimates made from a synthetic model (of dimensions 256 × 256, 8 km grid) using a fan wavelet (crosses), and periodogram estimates (circles).

[20] Although our ultimate aim is to perform full 3D inversion on our $\gamma_W^2(s, \mathbf{x})$ and $Q_W(s, \mathbf{x})$ functions, here we assume that local wavelet spectra are spatially "decoupled" [*Stark et al.*, 2003] so we can simply invert $\gamma_W^2(s, \mathbf{x}_0)$ for T_e at each grid point, $\mathbf{x}_0$ (assuming constant f), using the analytical formula for a uniform plate and a 1D search [*Press et al.*, 1992]. Solving for the load ratio f as well as T_e at each point requires joint inversion of the admittance and coherence. This is more difficult because wavelet admittance can be quite noisy at the roll-off wavelengths. Nevertheless, we have had some success with this and *Stark et al.* [2003] show that it is quite feasible by normalising the admittance. A more detailed discussion is beyond the scope of this paper.

[21] Applying this simple technique to the wavelet coherence data used to generate Figure 2 results in an apparent T_e variation with mean and SD of 24.5 ± 3.5 km. No mirroring or tapering of the grids was used, but the mean values were removed. For this data set the variation has a dominant wavelength of 500–1000 km, i.e., 2–4 times the flexural wavelength. This variation implies a natural limit on the T_e variations that can be mapped. We agree with *Lowry and Smith* [1994] that factor-of-2 changes can be considered significant.

[22] We have also carried out such tests for a number of non-uniform plate models. To allow comparison with the results of *Stark et al.* [2003] we have chosen a model with a square "bump" of T_e = 20 km embedded in a uniform plate of T_e = 10 km (Figure 3). Topography and gravity anomalies on a 10 km grid of size 128 × 128 were synthesised by finite differences, as previously described, and the wavelet coherence calculated from them. Figure 4 shows a "3D" view of this coherence, and Figure 5 shows the $T_e(\mathbf{x})$ resulting from the 1D inversion of $\gamma_W^2(s, \mathbf{x}_0)$ at each point $\mathbf{x}_0$, as described above. This result should be compared with Figure 18b of *Stark et al.* [2003], showing the half-coherence wavelength, rather than their Figure 18c (T_e) because they have inverted for both f and T_e whereas we have assumed f = 1. Our result appears somewhat closer to

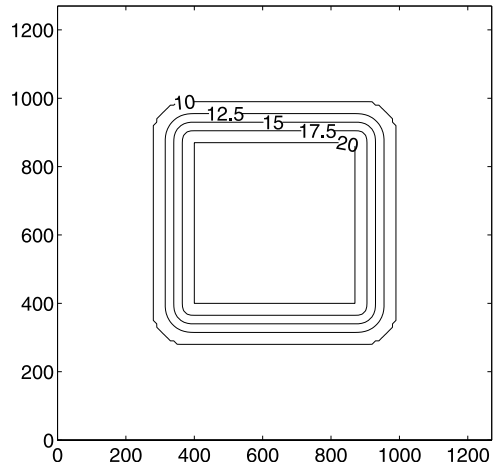

Figure 3. Contours of T_e in km for a "bump" model, with $f = 1$.

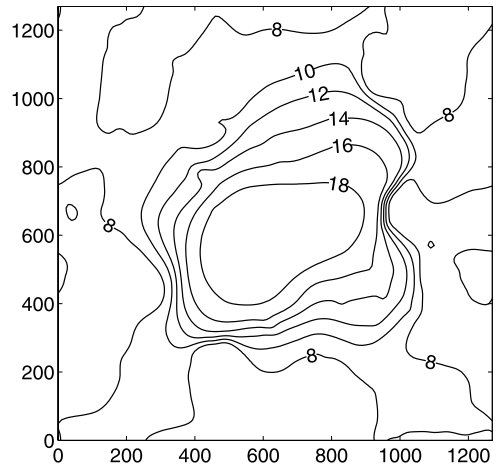

Figure 5. T_e distribution resulting from inversion of the wavelet coherence in Figure 4, assuming $f = 1$ and that each $\gamma^2_W(s, \mathbf{x}_0)$, at a particular location $\mathbf{x}_0$, can be modelled independently using the analytical formula for a uniform plate.

the true distribution, as theirs is much less concentrated. The mean and RMS of the differences between Figures 3 and 5 are -2.0 ± 1.7 km whereas *Stark et al.* [2003] quote 0 ± 5 km for their equivalent result (Figure 19a) – though it is not clear whether their error is RMS. They also state that there is no difference in accuracy whether they solve for both T_e and f together, or assume a fixed value for f, provided this is the correct value.

4. Conclusions

[23] For mapping isostatic parameters, the wavelet transform offers the important advantage of yielding local, as well as global, spectra, and hence can be used to map coherence and admittance, whereas the Fourier transform yields only global spectra. While it is true that a windowed Fourier transform (WFT), such as the multitaper method, can also be used to map spatial variations, the wavelet transform is superior because it effectively uses an optimal sized 'window' for each scale, while the WFT uses a single window size for all scales. However, the poor spatial localization of large scale wavelets means that T_e variations within thicker plates will be less well mapped than those within thinner plates, because the transition is at longer wavelengths for large T_e.

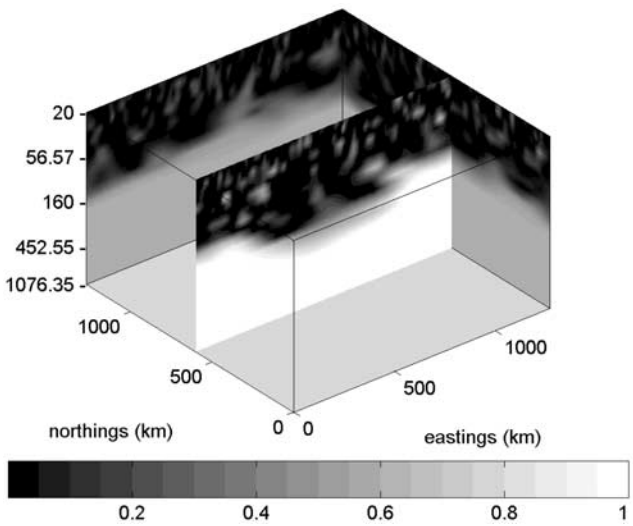

Figure 4. 3D coherence distribution, $\gamma^2_W(s, \mathbf{x})$, resulting from application of the fan wavelet transform to a pair of gravity/topography grids generated from the model in Figure 3. The vertical axis has been converted from scale to equivalent Fourier wavenumber, in km.

[24] Previous wavelets used for mapping T_e [*Stark et al.*, 2003] give coherence and admittance estimates that do not fit either those of analytical models or Fourier estimates, so that model predictions required the use of fractal models and complicated numerical integrals. We have shown that the use of the fan wavelet restores the simplicity of the Fourier method and allows the analytical expressions for coherence and admittance to be used (given the assumption of decoupling between local spectra).

[25] Furthermore, while the fan wavelet in this study was chosen to be isotropic, its azimuthal extent can be limited to reveal anisotropic T_e variations in any direction. Incidentally, the fan wavelet may be used in other areas of geophysics to generate an isotropic wavelet phase spectrum of any real-valued 2D data.

[26] **Acknowledgment.** This work was supported by the Australian Research Council (grant no. DP0211877) and a Curtin University Fellowship.

References

Bracewell, R. N. (1986), *The Fourier Transform and its Applications*, McGraw-Hill, New York.

Farge, M. (1992), Wavelet transforms and their applications to turbulence, *Annu. Rev. Fluid Mech.*, *24*, 395–457.

Forsyth, D. W. (1985), Subsurface loading and estimates of the flexural rigidity of continental lithosphere, *J. Geophys. Res.*, *90*, 12,623–12,632.

Kirby, J. F. (2004), Which wavelet best reproduces the Fourier power spectrum?, *Comput. Geosci.*, in press.

Lowry, A. R., and R. B. Smith (1994), Flexural rigidity of the Basin and Range–Colorado Plateau–Rocky Mountain transition from coherence analysis of gravity and topography, *J. Geophys. Res.*, *99*, 20,123–20,140.

Macario, A., A. Malinverno, and W. F. Haxby (1995), On the robustness of elastic thickness estimates obtained using the coherence method, *J. Geophys. Res.*, *100*, 15,163–15,172.

McKenzie, D., and J. D. Fairhead (1997), Estimates of the effective elastic thickness of the continental lithosphere from Bouguer and free air gravity anomalies, *J. Geophys. Res.*, *102*, 27,523–27,552.

Peitgen, H.-O., and D. Saupe (1988), *The Science of Fractal Images*, Springer, New York.

Pérez-Gussinyé, M., A. R. Lowry, A. B. Watts, and I. Velicogna (2004), On the recovery of effective elastic thickness using spectral methods: Examples from synthetic data and from the Fennoscandian Shield, *J. Geophys. Res.*, *109*, B10409, doi:10.1029/2003JB002788.

Poudjom Djomani, Y. H., J. D. Fairhead, and W. L. Griffin (1999), The flexural rigidity of Fennoscandia: Reflection of the tectonothermal age of the lithospheric mantle, *Earth Planet. Sci. Lett.*, *174*, 139–154.

Press, W. H., S. A. Teukolsky, W. T. Vetterling, and B. P. Flannery (1992), *Numerical Recipes in Fortran*, Cambridge Univ. Press, New York.

Stark, C. P., J. Stewart, and C. J. Ebinger (2003), Wavelet transform mapping of effective elastic thickness and plate loading: Validation using synthetic data and application to the study of southern African tectonics, *J. Geophys. Res.*, *108*(B12), 2558, doi:10.1029/2001JB000609.

Stewart, J. (1998), Gravity anomalies and lithospheric flexure: Implications for the thermal and mechanical evolution of the continental lithosphere, Ph.D. thesis, Dep. of Earth Sci., Oxford Univ., Oxford, U. K.

Swain, C. J., and J. F. Kirby (2003), The effect of "noise" on estimates of the elastic thickness of the continental lithosphere by the coherence method, *Geophys. Res. Lett.*, *30*(11), 1574, doi:10.1029/2003GL017070.

J. F. Kirby and C. J. Swain, Western Australian Centre for Geodesy, Curtin University of Technology, GPO Box 1987, Perth, WA 6845, Australia. (j.kirby@curtin.edu.au)